J Solid State Electrochem (2015) 19:2245–2253
DOI 10.1007/s10008-015-2836-5

ORIGINAL PAPER

Critical lithiation for C-rate dependent mechanical stresses in $LiFePO_4$

Cheng-Kai ChiuHuang[1] · **Hsiao-Ying Shadow Huang**[1]

Received: 5 December 2014 / Revised: 22 March 2015 / Accepted: 25 March 2015 / Published online: 24 April 2015

Abstract The prevention of capacity loss after electrochemical cycling is of paramount importance to the development of lithium-ion batteries, especially for applications in the electric vehicle industry. The objective of this research is to investigate C-rate dependent diffusion-induced stresses in electrode materials. $LiFePO_4$ is selected as the model system in this study since it is one of the most promising cathode materials used in electric vehicle applications. Finite element models incorporating several factors with concentration dependency are developed in this study including concentration-dependent anisotropic material properties, concentration-dependent and C-rate-dependent volume expansion coefficients, and concentration-dependent lithium ion diffusivity. Our simulation results show that the effect of concentration dependency on mechanical properties and lithium diffusivities cannot be neglected in mechanical stress predictions. We also observe that C-rate has a great effect on how fast the surface concentration is saturated, suggesting that C-rate dependency of the diffusion-induced stresses occurs at a critical lithiation stage: 47.5, 26.5, 10.1, and 6.8 % lithiation for 1, 2, 6, and 10 C, respectively. Mechanical stresses in perfect and cracked particles are also studied. It is observed that the crack surface orientation plays an important role in the diffusion-induced stress. The existence of the crack surface increases mechanical stresses, suggesting that particles inside the material may undergo fractures faster and may accelerate the material deterioration, leading to capacity loss at higher C-rate (dis)charging.

Keyword Diffusion-induced stresses · Lithium-ion batteries · Concentration gradient · Crack · Finite element method

✉ Hsiao-Ying Shadow Huang
hshuang@ncsu.edu

[1] Mechanical and Aerospace Engineering Department, North Carolina State University, R3158 Engineering Building 3, Campus Box 7910, 911 Oval Drive, Raleigh, NC 27695, USA

Introduction

Lithium-ion batteries with high energy densities and high-rate capabilities have been selected as the main energy storage devices in the electrical vehicle industry [1, 2]. Maintaining the high rate performance is critical for lithium-ion battery applications. Olivine-based lithium iron phosphate ($LiFePO_4$) with an orthorhombic crystal structure is one of the most promising cathode materials because $LiFePO_4$ demonstrates excellent characteristics for applications in EVs/PHEVs such as low raw material cost, good thermal stability, abundant iron resources, flat charge/discharge curves, and a high theoretical energy density (170 mAh g^{-1}) [3–5]. It has been reported that $LiFePO_4$ functions as a two-phase system at room temperature under low C-rate conditions, while both the lithium-rich phase (LFP) and lithium-poor phase (FP) have a narrow solid solution range [6–10]. However, capacity loss has been observed at high C-rates or after a long period of cycling [2, 11–13].

In $LiFePO_4$, the phase transition mechanism between the LFP and FP phases has been suggested to be C-rate dependent via theoretical predictions [14] and experimental observations [11, 12]. A higher C-rate means that more lithium ions (i.e., higher lithium-ion mass flux) need to be pumped into cathode materials quickly [15]. Thus, there is less time for lithium ions to exchange with the neighboring particles to reach a lower free energy, an equilibrium phase separation state [11, 12]. Bai et al. [14] used a one-dimensional phase field model to predict the suppression of two-phase separation when the C-rate is above a critical value. Tang et al. [16] used a diffuse-interface model to predict the phase transformation pathway for $LiFePO_4$ and related these results to the overpotential and particle sizes. It

was concluded that strain energy is an extra energy barrier and should be overcome during lithiation. They have observed that higher underpotential at high C-rate discharging is the driving force for conquering this energy penalty [11, 12]. This high strain energy also explains why the nonequilibrium solid solution phase is unstable under high C-rates.

Recently, Orikasa et al. [11, 17] used in situ time-resolved X-ray diffraction (XRD) to monitor the structural evolution during cycling ranging from 1 to 10 C. The XRD patterns show that a solid solution phase $Li_{x\approx0.6}FePO_4$ (x represents the lithium ion concentration in the host structure and ranges between 0 to 1 for the Li_xFePO_4 system) starts to evolve after 5 C and becomes a fully solid solution phase transition pathway at 10 C. However, this intermediate solid solution phase is unstable and will separate into two single FP and LFP phases after the termination of charging/discharging. Later, Zhang et al. [12] used in situ synchrotron XRD to monitor the structural changes in commercial nanoparticle (140 nm) $LiFePO_4$ batteries during charge/discharge with C-rates varying between 0.2 and 60 C. Similarly, a weak intermediate reflection of the solid solution Li_xFePO_4 phase could be detected at 5 C in the initial 5 % charge. For 60 C, a significant intensity fluctuation between LFP and FP reflections was observed, suggesting that the phase transition at high C-rates does not obey the equilibrium phase separation path. Their experimental results also confirm that this intermediate solid solution phase (Li_xFePO_4) is very unstable, and the phase separation occurs only 10 s after relaxation. Liu et al. [18] performed synchrotron high-energy XRD to measure the structural volume changes at different C-rates (0.1 to 5 C) for commercial $LiFePO_4$ batteries with a mean particle size of 62.5 nm. The results suggest that the phase transition behavior is a combination of a two-phase reaction with a single solid solution path. However, the phase transition under high C-rates is dominated by the solid solution path. Moreover, Li et al. [19] used synchrotron-based X-ray microscopy to observe the lithium-ion intercalation behavior in samples including over 3000 $LiFePO_4$ particles. The experimental results show that during discharging, the lithium-ion insertion mechanism will change from a particle-by-particle intercalation at low C-rates (e.g., 0.02 and 1.5 C) to a concurrent insertion behavior at high C-rates (e.g., 5 C). The chemical potential and phase transformation behavior under high C-rates for porous electrode materials are then delineated by nonequilibrium thermodynamics [20, 21], in which the coherency strains play an important role in the suppression of phase separation at high C-rates [22].

Garcia et al. [15] used a 1D finite element model to predict diffusion-induced stresses, and the results show that fast discharging (higher mass flux) will result in higher stress. Diffusion-induced stresses in single spherical, cylindrical, or ellipsoidal particles have been extensively discussed by assuming isotropic material properties [23–26]. In our previous study, we investigated the stress evolution on the phase boundary in a single $LiFePO_4$ particle [27]. The maximum stress occurs on the particle surface during lithiation, explaining the experimentally observed particle fracture. Further, the voltage fluctuation is more noticeable in 10 C samples as compared to other ones with low C-rates, possibly suggesting that a different lithium insertion mechanism occurs at high C-rates [28]. Thus, to investigate strain energy under different C-rates may be helpful for explaining the observed voltage fluctuation.

To better understand the effect of C-rate on the diffusion-induced stress in $LiFePO_4$ cathode material, a model that incorporates the concentration-dependent anisotropic material properties, the C-rate dependent volume expansion coefficient, and concentration-dependent lithium-ion diffusivity are required. Therefore, in the current study, we establish a finite element model incorporating the aforementioned factors to predict the C-rate dependent diffusion-induced stress. The lithium-ion concentration profiles, stresses, and elastic strain energy during lithiation at different C-rates are compared and discussed.

Particle fractures and crack growth in $LiFePO_4$ have been observed after charge/discharge cycling [29], and it is suggested that crack-induced capacity loss is strongly related to the mechanical stress [3, 30]: the crack surface makes the active material lose contact with other active materials and the electrolyte, leading to the blockage of electron transfer that damages capacity [31]. Various studies have investigated the causes of particle fracturing by calculating the diffusion-induced stresses based on single spherical, ellipsoidal, or irregularly shaped particles [23, 32–38]. It has been suggested that stress levels within particles are related to the particle morphology, anisotropic material properties, phase transition-induced mechanical property changes, and particle size for the $LiCoO_2$ system [32, 39]. Moreover, Woodford et al. [40, 41] proposed design criteria to prevent particle fracturing (i.e., electrochemical shock) by minimizing the principal shear strain. Zhu et al. [33] showed that the crack located at the center of a spherical $LiMn_2O_4$ particle experiences higher stresses than those at other locations. However, the effect of the crack surface orientation on the lithium concentration profiles and stress levels has not been reported. In the current study, we further conduct finite element analyses to understand how the crack orientation affects the concentration profile and diffusion-induced stress during lithiation. The results from the current study provide a better understanding of the relationship between high C-rate charge/discharge and the observed capacity loss due to particle fracturing.

Method

We used a thermal stress analysis approach [27] to investigate C-rate dependent diffusion-induced stresses during lithiation in $LiFePO_4$ electrode material. The study on the diffusion-induced stresses based on the thermal analogy has been wildly discussed [26, 32, 35, 42]. However, concentration-dependent

diffusivity, C-rate dependent volume expansion, C-rate dependent critical lithiation, and the coupled mechanical effects of $LiFePO_4$ have not been considered as a whole. In this study, the thermal diffusivity is used to represent the lithium-ion diffusivity. The heat flux is used to represent the mass flux of lithium-ions (J), and the temperature gradient represents lithium-ion concentration gradient. Since a commercial $LiFePO_4$ battery is a layered structure composed of a cathode strip and an anode strip with a separator between them [43], 1D lithium-ion mass flux J along the Y-axis is used as the driving force for the system (Fig. 1a). As a result, lithium-ion concentration varies continuously inside the material along the direction of lithium-ion mass flux J.

To investigate the C-rate dependency, C-rates are controlled by different mass fluxes J and a two-step simulation approach is used. We first simulated lithium-ion mass flux J on the interface of electrode and separator, and lithium-ion mass flux diffusing into the cathode material at different C-rates is described by Chiang's group [15] and Lim et al. [39]. When the surface between the separator and the cathode is saturated, the second step diffusion process starts. Further lithium-ion insertion without the boundary condition confinement will cause the lithium-ion concentration to exceed its maximum value (i.e., $x>1$ for Li_xFePO_4). Thus, we confine the surface concentration to be 1 to continue the lithiation process in the second step.

That is, Fick's first law of diffusion is used in the first step, and Fick's second law with a fixed surface concentration $\phi(y,t)=\phi(0,t)=1$ is used in the second step to serve as the driving force of the lithium ion diffusion:

$$J = -D\nabla\phi = -D\frac{\partial\phi}{\partial y} \text{ and} \frac{\partial\phi}{\partial t} = D\left(\frac{\partial^2\phi}{\partial y^2}\right) \quad (1)$$

where D is the lithium ion diffusivity, and $\phi(y, t)$ is the time-dependent lithium-ion concentration profile along the diffusion direction, i.e., the y-axis. Of note, in the current study, we focus on the stresses in the cathode material, and we assume it is a continuous media. Therefore, the electrolyte and anode materials are not included in the model. In addition, the porous microstructure and the exchange of lithium-ions between single $LiFePO_4$ particles are not considered in this study.

ANSYS Multiphysics (ANSYS, Inc., Canonsburg, Pennsylvania, USA) is used to develop a thermal-static coupling finite element model to investigate the diffusion-induced stresses under various C-rate conditions. A 10 μm×10 μm×10 μm cubic finite element model containing 1000 elements was developed per our previous study, in which a 10 μm×10 μm sputtering area was used to measure the lithium ion intensities in $LiFePO_4$ strip [28]. Various C-rates are chosen by assigning different mass fluxes J, where the 1 C model has $J_{1\ C}=0.225\ W\ m^{-2}$, the 2 C model has $J_{2\ C}=0.45\ W\ m^{-2}$, the 6 C model has $J_{6\ C}=1.35\ W\ m^{-2}$, and the 10 C model has $J_{10\ C}=2.25\ W\ m^{-2}$, respectively. The value of $J_{1\ C}=0.225\ W\ m^{-2}$ is chosen in our simulation to ensure enough time for lithium ion concentration to be saturated on the flux surface. Since lithium-ion concentration x varies between 0 and 1 in Li_xFePO_4 during lithiation, the maximum concentration on the particle surface is 1. Due to different C-rates, the time required for the lithium ion concentration to reach the stoichiometric maximum ($x=1$) on the flux surface changes accordingly. Therefore, the concentration profiles $\phi(y, t)$, the resulting concentration gradient $\nabla\phi = \frac{\partial\phi}{\partial y}$, and the Laplacian $\nabla^2\phi = \frac{\partial^2\phi}{\partial y^2}$ behave differently for each C-rate model. Once the concentration on the flux surface is saturated for each C-rate model, the finite element simulation switches to the next step.

In step two, Fick's second law with a fixed surface concentration $\phi(y,t)=\phi(0,t)=1$ is used to serve as the driving force of the lithium ion diffusion, $\frac{\partial\phi}{\partial t} = D\left(\frac{\partial^2\phi}{\partial y^2}\right)$, as shown in Fig. 1. To calculate the lithiation during the simulation, a trapezoidal rule is used with a uniform grid. The amount of lithiation is the

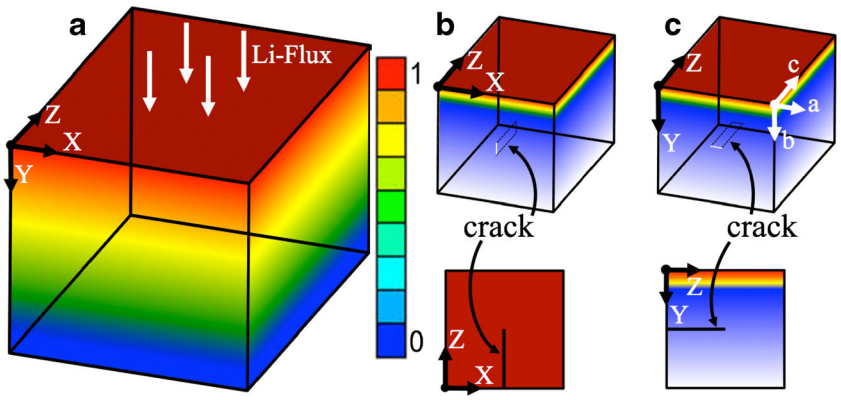

Fig. 1 A 1000-μm^3 $LiFePO_4$ model with a one-dimensional lithium mass flux along the y-axis. An assigned mass flux ($J_{1C}=0.225\ W\ m^{-2}$) is used to mimic the discharging of different C-rates. Concentration-dependent material properties, lithium diffusivity, and C-rate dependent volume expansion coefficients are incorporated in the simulation. **a** Models with no crack. **b** Models with a crack surface parallel to (100) (i.e., parallel to the Li flux direction). **c** Models with a crack surface parallel to (010) (i.e., perpendicular to the Li flux direction). The crack size is assumed to have a length of 5 μm, a width of 2 μm, and a thickness of 0.2 μm. *Colored legend*: high lithium ion concentration is in *red* and low lithium ion concentration is in *blue*

accumulated sum of each trapezoid between two consecutive data points, and the percentage of lithiation is calculated by normalizing with the Riemann sum [44].

To derive diffusion-induced stress σ due to the lithiation of $LiFePO_4$, we start by taking an isotropic material under temperature gradient as an example; the thermal stress of an isotropic material is calculated from two sources: the first source is from the deformation of the materials and the second source is from the temperature differences. Therefore, the stress-strain-temperature relation could be expressed as follows: $\sigma_{ij}=2\mu\varepsilon_{ij}+\lambda\varepsilon_{kk}\delta_{ij}-\alpha(3\lambda+2\mu)(\Delta T)\delta_{ij}$, where μ and λ are Lame's constants, δ is Kronecker delta, α is coefficient of thermal expansion, and ΔT are temperature differences. By setting $i=j=k$, we could simplify the equation above as follows: $\sigma_{kk}=(3\lambda+2\mu)[\varepsilon_{kk}-3\alpha(\Delta T)]$. Of note, if there are no temperature changes for the said materials, there are still mechanical stresses in the material.

Analogously, as for the anisotropic $LiFePO_4$, the materials property is represented by $[C]_T$, the coherent interface during the phase transformation results in strain fields $[\varepsilon]$ due to simply two materials mismatch [8]. The concentration differences $\Delta\phi$ inside $LiFePO_4$ produce diffusion-induced stresses, and they are calculated by the concentration gradient $\nabla\phi$ with the volume expansion coefficient ($\Delta V=3\alpha$) due to diffusion. From available experimental data [18], we have observed that volume expansion coefficient is C-rate dependent. For example, $\Delta V\approx 3\alpha$=5.6, 5.25, 4.7, and 4.3 % for 1, 2, 6, and 10 C, respectively.

As such, we have generalized our diffusion-induced stress σ equation as follows:

$$[\sigma] = [C]_T([\varepsilon]-3\alpha\nabla\phi) \tag{2}$$

Likewise, if there are no concentration gradients inside the $LiFePO_4$, there are still mechanical stresses in the material due to the coherency between two phases [8]. In our model, α and ϕ are unitless because the lithium-ion concentration has been normalized ($0\le\phi\le1$). The strain energy from the finite element analysis is formulated as $U=\int\sigma d\varepsilon$, where the total strain energy U is the summation of the strain energy of each element.

Concentration-dependent diffusivity

To better capture the diffusion-induced stresses in $LiFePO_4$, several additional factors are considered in the current study. First, we incorporate concentration-dependent diffusivity D in both of Fick's diffusion laws. It is observed that lithium ion diffusion in the $FePO_4$ phase is faster than that in the $LiFePO_4$ phase, $D_{FePO4}/D_{LiFePO4}=6$ [45], and the diffusion coefficient $D_{LiFePO4}=1.6\times10^{-12}$ m^2 s^{-1} is used in this study [46]. Previous study [47] showed that the assumption of linear relationship of Fickian diffusion coefficient between the Li-poor and Li-rich phase makes good prediction of the potential profiles. Thus, in this study, a linearly concentration-dependent diffusivity is assumed as follows:

$$D(x) = x[D_{LiFePO_4}] + (1-x)[D_{FePO_4}], \tag{3}$$

where x represents lithium ion concentration ($0\le x\le1$).

Concentration-dependent elastic moduli for randomly distributed particles

To incorporate the concentration-dependent anisotropy material properties of the $LiFePO_4$ system, $[C(x)] = x[C]^{LiFePO_4} + (1-x)[C]^{FePO_4}$ is used [27, 48], where $[C]$ is the stiffness matrix in the finite element analyses. Orthorhombic elastic constants of both phases $[C]^{LiFePO_4}$ and $[C]^{FePO_4}$ are obtained from Maxisch and Ceder [49]. Moreover, $LiFePO_4$ particles are generally distributed randomly in the electrode material [50]. It has been suggested that for a polycrystalline material, the effective Young's modulus and effective Poisson's ratio could be calculated by averaging all possible orientations of single grains [51]. Rather than assuming a perfect isotropic material property, in this study, we considered six different particle orientations to derive the average elastic constants of the stiffness matrix $[C(x)]_T$ to capture the particles' random distribution in Eq. 2. A transformation matrix $[C(x)]_T=[T_{ij}]^{-1}[C(x)][T_{ij}]$ is used [52], where:

$$[T_{ij}] = \begin{pmatrix} {m_1}^2 & {n_1}^2 & {p_1}^2 & 2n_1p_1 & 2p_1m_1 & 2m_1n_1 \\ {m_2}^2 & {n_2}^2 & {p_2}^2 & 2n_2p_2 & 2p_2m_2 & 2m_2n_2 \\ {m_3}^2 & {n_3}^2 & {p_3}^2 & 2n_3p_3 & 2p_3m_3 & 2m_3n_3 \\ m_2m_3 & n_2n_3 & p_2p_3 & n_2p_3+n_3p_2 & p_2m_3+p_3m_2 & m_2n_3+m_3n_2 \\ m_3m_1 & n_3n_1 & p_3p_1 & n_3p_1+n_1p_3 & p_3m_1+p_1m_3 & m_3n_1+m_1n_3 \\ m_1m_2 & n_1n_2 & p_1p_2 & n_1p_2+n_2p_1 & p_1m_2+p_2m_1 & m_1n_2+m_2n_1 \end{pmatrix} \text{ and}$$

$$\begin{bmatrix} m_1 & n_1 & p_1 \\ m_2 & n_2 & p_2 \\ m_3 & n_3 & p_3 \end{bmatrix} = \begin{bmatrix} \cos\theta_{x1} & \cos\theta_{y1} & \cos\theta_{z1} \\ \cos\theta_{x2} & \cos\theta_{y2} & \cos\theta_{z2} \\ \cos\theta_{x3} & \cos\theta_{y3} & \cos\theta_{z3} \end{bmatrix}, \text{ in which}$$

(*1*, *2*, *3*) and (x, y, z) represent the coordinates before and after the orientation, respectively; (m, n, p) are direction cosines. The elastic constants of the stiffness matrix after averaging the six possible particle orientations are listed in Table 1. Besides, an isotropic volume expansion with a C-rate dependency diffusion mechanism is further considered in this model.

Table 1 Elastic constants after averaging six-particle orientations

Phase	Elastic constants (GPa)								
	C_{11}	C_{22}	C_{33}	C_{44}	C_{55}	C_{66}	C_{12}	C_{13}	C_{23}
$FePO_4$	137.4	146.0	132.0	40.8	38.2	42.1	41.0	29.1	29.1
$LiFePO_4$	164.3	162.9	181.1	40.8	40.5	43.9	61.1	54.9	67.7

C-rate-dependent volume expansion

It has been reported that the volume change between LFP and FP phases decreases from ΔV=6 % at 0.1 C to ΔV=4.8 % at 5 C, while increasing the C-rate discharging increases the solid solution range [18]. With the goal of better modeling the C-rate dependent diffusion-induced stresses, we used extrapolation to derive isotropic volume expansion coefficients α at different C-rates with the assumption that high order terms are negligible, $\Delta V \approx 3\alpha$=5.6, 5.25, 4.7, and 4.3 % for 1, 2, 6, and 10 C, respectively, is used in Eq. 2 from available experimental data [18], where $\alpha_a=\alpha_b=\alpha_c=\alpha$ and a, b, c are lattice vectors. Of note, the experimental volume changes are based on the ensemble of $LiFePO_4$ particles. Thus, the volume change throughout the sample may not be smooth since the miscibility gap is particle size dependent [7]. For the case of considering the porous structure and lithium-ion exchanges between single particles, the application of constant volume expansion coefficient may not be valid.

In this study, we further hypothesize that crack orientations could alter concentration profiles and resulting diffusion-induced stresses in $LiFePO_4$ particles. Therefore, two additional models with two distinct crack orientations are considered. Crack surfaces parallel to the (100) and (010) planes are generally observed in the electrochemically cycled $LiFePO_4$ [53]. Therefore, two additional models with two distinct crack orientations are considered: (1) the crack surface parallel to (100) (i.e., parallel to the Li flux direction) as shown in Fig. 1b, and (2) the crack surface parallel to (010) (i.e., perpendicular to the Li flux direction) as shown in Fig. 1c. The crack size is assumed to have a length of 5 μm, a width of 2 μm, and a thickness of 0.2 μm. Of note, for the purpose of comparing concentration profiles in the region far away from the crack region, the crack surface is designed to only extend to the midpoint of the model and does not go through the whole model.

Results and discussion

Several studies investigate diffusion-induced stresses in single particles by using a constant diffusivity throughout the lithiation [24, 26, 32, 33, 39, 54]. However, theoretical calculation indicates that lithium ion diffusion in the Li-poor phase is faster than that in the Li-rich phase [46, 55], and the ratio of $D_{FePO4}/D_{LiFePO4}$=6 has been reported [45]. As such, we first investigated the effect of concentration-dependent diffusivity on concentration profiles $\phi(y, t)$, as shown in Fig. 2. Red lines show the results of using a constant diffusivity ($D_{LiFePO4}=D_{FePO4}=1.6\times10^{-12}$ m^2 s^{-1} [46]) throughout the lithiation stage, and blue lines show the results of considering a concentration-dependent diffusivity, as shown in Eq. 3. The dashed lines are concentration profiles at 20 % lithiation, and the solid lines represent the concentration profiles at 50 % lithiation. It is observed that by considering the concentration dependency in diffusivity constants, larger concentration gradients are observed, and this effect is more noticeable at a higher lithiation stage (i.e., 50 vs. 20 %). Similar observations are reported in other battery material systems wherein $LiCoO_2$ [34, 39] and $LiMn_2O_4$ [33] were modeled as single particles with the assumption of isotropic material properties. The result shown in Fig. 2 suggests that to better predict the diffusion-induced stresses for electrode materials, it is necessary to incorporate concentration-dependent diffusivity, especially for materials with a significant change in diffusivity between the lithium-rich and lithium-poor phases.

The comparison of concentration profiles $\phi(y, t)$ between different C-rates at the same initial lithiation stage (5 %) is shown in Fig. 3a. Increases in the concentration gradient near the flux surface with increasing C-rates is observed. Figure 3b compares the concentration profiles and lithiation stages at different C-rates when the surface concentration is saturated. The results show that C-rate has a great effect on how fast the surface concentration is saturated, and the corresponding critical lithiation stages for 1, 2, 6, and 10 C are 47.5, 26.5, 10.1,

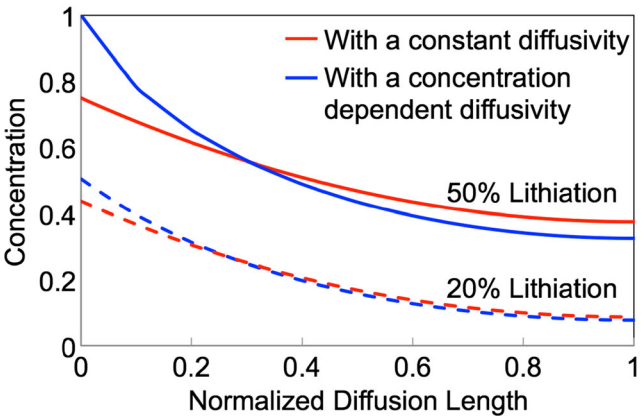

Fig. 2 The effect of concentration-dependent diffusivity on the concentration profiles during lithiation. *Red lines* are the results from assuming a constant diffusivity ($D_{LiFePO4}$), and *blue lines* are the results from considering a concentration-dependent diffusivity. The diffusivity varies between D_{FePO4} and $D_{LiFePO4}$ and the ratio of $D_{LiFePO4}/D_{FePO4}$=1/6. The *dashed lines* are the concentration profiles at 20 % lithiation, and the *solid lines* are the concentration profiles at 50 % lithiation. The results show that the effect of concentration-dependent diffusivity becomes more significant at a higher lithiation stage

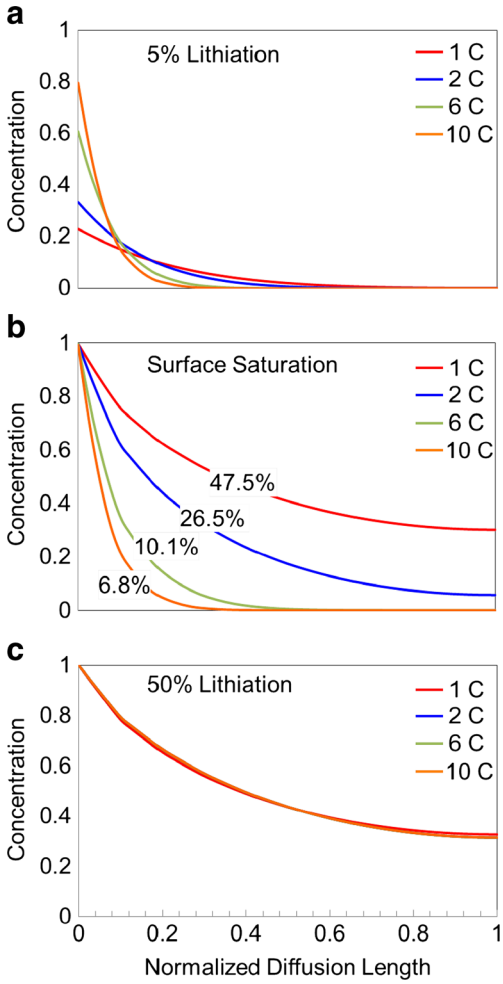

Fig. 3 The evolution of concentration profiles at different C-rates along the diffusion direction of *y*-axis. **a** Concentration profiles at 5 % lithiation. A higher C-rate results in a larger concentration gradient at the same amount of lithiation. **b** Concentration profiles for different C-rates when the surface concentration is saturated (equal to 1 in our model system). The result shows that the surface concentration is saturated more quickly at higher C-rates as compared to lower C-rates. The corresponding critical lithiation for 1, 2, 6, and 10 C when the surface concentration is saturated are 47.5, 26.5, 10.1, and 6.8 %, respectively. **c** After around 50 % lithiation, the evolution of concentration profiles becomes C-rate independent

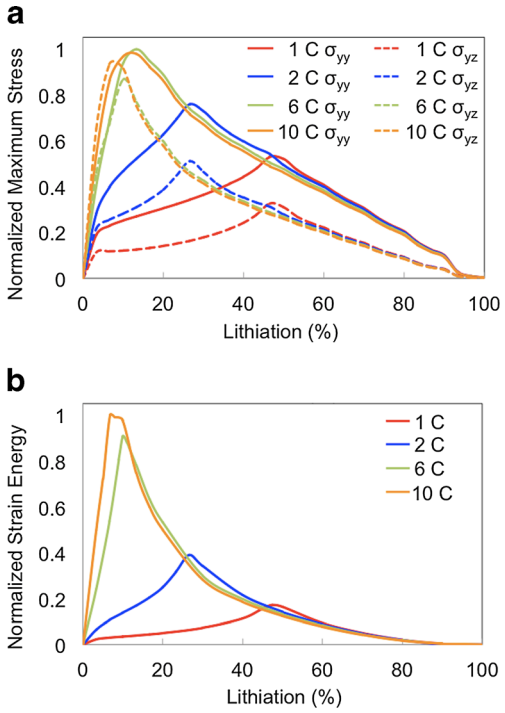

Fig. 4 **a** Normalized maximum normal stress (σ_{YY}) and shear stress (σ_{YZ}) during lithiation. The lithium flux is along the *y*-axis during the simulation. The *solid lines* are for σ_{YY} and the *dashed lines* are for σ_{YZ}. It is observed that a higher C-rate results in a higher maximum stress during lithiation. The maximum stress occurs very close to critical lithiation when the surface concentration is saturated, suggesting a larger concentration gradient at higher C-rates could result in higher maximum stresses. **b** The C-rate dependent strain energy evolution during a complete lithiation cycle. A higher C-rate results in a higher strain energy and can be considered as an energy barrier that needs to be overcome during lithiation. The maximum strain energy occurs very close to critical lithiation when the surface concentration is saturated. Thus, the higher strain energy in the material is caused by a larger concentration gradient at high C-rates

and 6.8 % respectively. However, after 50 % lithiation, the concentration profile becomes C-rate independent (Fig. 3c).

Figure 4a compares the normalized maximum normal stress (σ_{YY}) and shear stress (σ_{YZ}) at different C-rates during lithiation. Increased mechanical stresses inside the material with increasing C-rates are observed during the lithiation process. It is observed that peak stresses generally occur when the surface concentration reaches saturation, i.e., 47.5, 26.5, 10.1, and 6.8 % lithiation for 1, 2, 6, and 10 C, respectively, as shown in Fig. 3b, suggesting a larger concentration gradient $\nabla\phi$ could lead to higher stress levels inside the materials. Of note, the peak stress does not happen at the 100 % lithiation stage (Fig. 4a). The phenomenon of initially increasing stresses followed by a decreased one is also observed in $LiCoO_2$ [39] and $LiMn_2O_4$ [33] battery chemistries. The results from our study further confirm that for lithium insertion materials, the peak stress depends mainly on the critical lithiation stages. The ratios of the normalized maximum normal stresses (σ_{YY}) are 0.53:0.76:0.98:1 for 1, 2, 6, and 10 C, respectively (Fig. 4a), suggesting that diffusion-induced stresses are not linearly proportional to C-rates. Furthermore, we observe similar stress profiles from 6 and 10 C models, and it is suggested that for materials subjected to large diffusion-induced stresses, a threshold C-rate may exist (6 C in this study).

C-rate-dependent strain energy evolution during a complete lithiation cycle is shown in Fig. 4b. Our results show that due to larger concentration gradients, higher C-rates could result in higher strain energies. This observation is similar to that reported in a core-shell model by Deshpande et al. [25], where the strain energy initially increases during lithiation, and then decreases after reaching its peak value. Similarly, as shown by the stress profiles in Fig. 4a, the maximum total strain energy occurs (Fig. 4b) at critical lithiation when the concentration is saturated on the flux surface (Fig. 3b). That

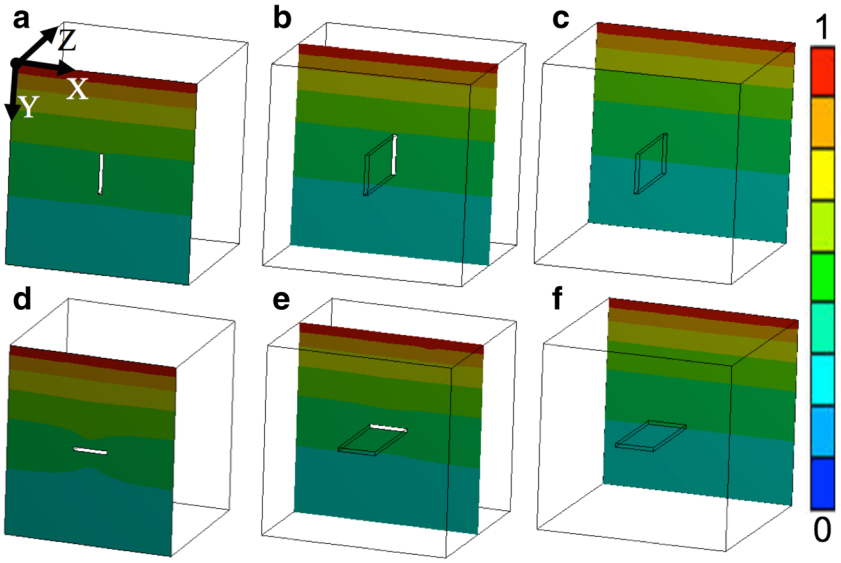

Fig. 5 The effect of crack orientation on the concentration patterns (1 C model with 50 % lithiation). **a**–**c** The concentration profiles in the front, middle, and back cross-sections of the model when the crack surface is parallel to the Li-flux. An insignificant change in the concentration pattern is observed. **d**–**f** The concentration profiles in the front, middle, and back cross-sections of the model when the crack surface is normal to the Li-flux. A higher concentration variation near the crack surface is observed. *Colored legend*: high lithium ion concentration is in *red* and low lithium ion concentration is in *blue*

is, the strain energy drops quickly after reaching the required critical lithiation stages for each C-rate. It should be noticed that after about 30 % lithiation, the strain energies in the 6 and 10 C models already become lower than those in the 2 C model.

Figure 5 shows the comparison of the concentration profiles between the crack surface parallel to the Li-flux (Fig. 1b) and the crack surface normal to the Li-flux (Fig. 1c) at 50 % lithiation in the 1 C model. We observed that the preexisting crack surface blocks lithium diffusion, thus affecting the concentration profiles and associated stresses. The results show that the concentration profiles are affected more noticeably when the crack surface is normal to the lithium flux (Fig. 5d, e) as compared to the model with the crack surface parallel to the lithium flux (Fig. 5a, b). However, for materials that are located far from the crack surface (Fig. 5c, f), the concentration profiles are not altered by the cracks.

Figure 6 compares maximum stresses σ_{YY} and σ_{XX} for 1 and 10 C models in three cases: (1) particles with no cracks, (2) particles with a crack surface parallel to the Li-flux

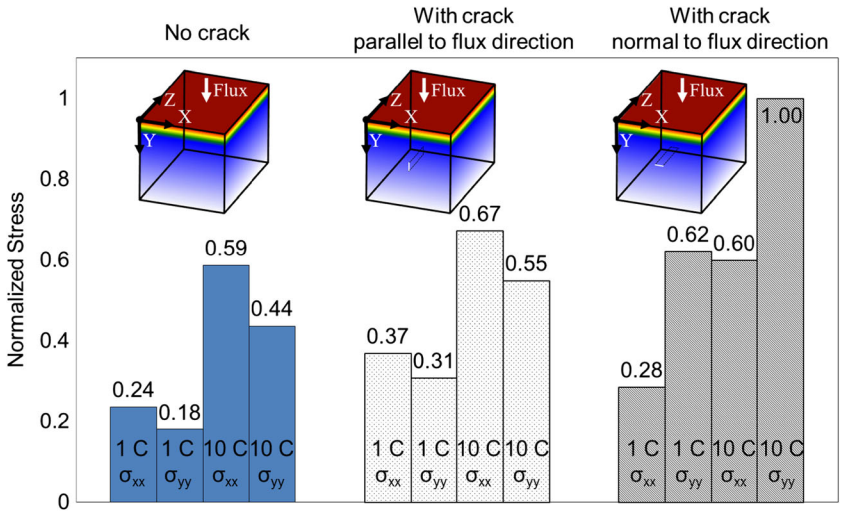

Fig. 6 A comparison of maximum stress σ_{XX} and σ_{YY} in 1 and 10 C models of three cases: (1) Models with no cracks, (2) models with a crack surface parallel to the Li-flux, and (3) models with a crack surface normal to the Li-flux. It is observed that a higher C-rate results in higher stress. Also, the crack surface causes higher stress. For the crack surface parallel to the Li-flux, σ_{XX} is higher than σ_{YY} (in both the 1 and 10 C models) and σ_{XX} could result in a mode I fracture. However, for the crack surface normal to the Li-flux, σ_{YY} becomes larger than the σ_{XX} (in both the 1 and 10 C models) and σ_{YY} could result in a mode I fracture in this case

direction, and (3) particles with a crack surface normal to the Li-flux direction. It is observed that a higher C-rate results in higher maximum stresses. Further, particles with cracks also demonstrated higher stress in the materials. We also observed that the orientation of the crack affects stress states in the materials. For example, for models with a crack surface parallel to the Li-flux direction, σ_{XX} is observed to be higher than σ_{YY} in both the 1 and 10 C models, and σ_{XX} could result in a mode I fracture. In contrast, for models with a crack surface normal to the Li-flux direction, σ_{YY} becomes higher than σ_{XX} in both the 1 and 10 C models, and σ_{YY} could result in a mode I fracture in that case. Although both crack surfaces are dominated by mode I fractures, the crack surface normal to the Li-flux direction still results in a higher stress state and this is due to the concentration profile varying along the direction of Li-flux. This result shows that both C-rate and crack surfaces could increase internal stresses in the materials and may accelerate material deterioration after cycling.

Conclusion

Finite element models incorporating several factors with the concentration dependency are developed in this study including concentration-dependent anisotropic material properties, concentration-dependent and C-rate-dependent volume expansion coefficients, and concentration-dependent lithium ion diffusivity. A higher lithium flux will result in a larger concentration gradient inside the materials, and increased mechanical stresses and elastic strain energies are observed with increased C-rates (i.e., flux). Our results also show that C-rate has a great effect on how fast the surface concentration becomes saturated, and it is concluded that C-rate dependency on the diffusion-induced stresses occurs at a critical lithiation stage when the concentration is fully saturated on the flux surface: 47.5, 26.5, 10.1, and 6.8 % lithiation for 1, 2, 6, and 10 C, respectively. Furthermore, our results show that the concentration profiles are significantly affected when the crack surface is normal to the lithium flux and mode I fractures dominate inside materials. Thus, high stresses due to fast charging/discharging may accelerate the crack surface growth, leading to capacity loss after cycling.

References

1. Chiang YM (2010) Science 330:1485–1486
2. Kang B, Ceder G (2009) Nature 458:190–193
3. Yuan LX, Wang ZH, Zhang WX, Hu XL, Chen JT, Huang YH, Goodenough JB (2005) Energy Environ Sci 4:269–284
4. Zhang WJ (2011) J Power Sources 196:2962–2970
5. Wang YX, Huang HYS (2012) TSEST Trans Control Mech Sys 1(5):192–200
6. Meethong N, Kao YH, Tang M, Huang HYS, Carter WC, Chiang YM (2008) ACS Chem Mat 20:6189–6198
7. Meethong N, Huang HYS, Carter WC, Chiang YM (2007) Electrochem Solid-State Lett 10:A134–A138
8. Meethong N, Huang HYS, Speakman SA, Carter WC, Chiang YM (2007) Adv Funct Mater 17:1115–1123
9. Kao YH, Tang M, Meethong N, Bai J, Carter WC, Chiang YM (2010) Chem Mat 22:5845–5855
10. Kobayashi G, Nishimura SI, Park MS, Kanno R, Yashima M, Ida T, Yamada A (2009) Adv Funct Mater 19:395–403
11. Orikasa Y, Maeda T, Koyama Y, Murayama H, Fukuda K, Tanida H, Arai H, Matsubara E, Uchimoto Y, Ogumi Z (2013) J Am Chem Soc 135:5497–5500
12. Zhang X, Hulzen MV, Singh DP, Brownrigg A, Wright JP, Dijk NHV, Wagemaker M (2014) Nano Lett 14:2279–2285
13. Zhang Y, Wang CY, Tang X (2011) J Power Sources 196:1513–1520
14. Bai P, Cogswell DA, Bazant MZ (2011) Nano Lett 11:4890–4896
15. Garcia RE, Chiang YM, Carter WC, Limthongkul P, Bishop CM (2005) J Electrochem Soc 152:A255–A263
16. Tang M, Huang HYS, Meethong N, Kao YH, Carter WC, Chiang YM (2009) ACS Chem Mater 21:1557–1571
17. Orikasa Y, Maeda T, Koyama Y, Minato T, Murayama H, Fukuda K, Tanida H, Arai H, Matsubara E, Uchimoto Y, Ogumi Z (2013) J Electrochem Soc 160:A3061–A3065
18. Liu Q, He H, Li ZF, Liu Y, Ren Y, Lu W, Lu J, Stach EA, Xie J (2014) ACS Appl Mater Interfaces 6:3282–3289
19. Li Y, Gabaly FE, Ferguson TR, Smith RB, Bartelt NC, Sugar JD, Fenton KR, Cogswell DA, Kilcoyne ALD, Tyliszczak T, Bazant MZ, Chueh WC (2014) Nat Mater 13:1149–1156
20. Ferguson TR, Bazant MZ (2012) J Electrochem Soc 159:A1967–A1985
21. Bazant MZ (2013) Acc Chem Res 46:1144–1160
22. Cogswell DA, Bazant MZ (2012) ACS Nano 6:2215–2225
23. Christensen J, Newman J (2006) J of Solid State Electrochem 10: 293–319
24. Cheng YT, Verbrugge MW (2009) J Power Sources 190:453–460
25. Deshpande R, Cheng YT, Verbrugge MW, Timmons A (2011) J Electrochem Soc 158:A718–A724
26. Zhang X, Shyy W, Sastry AM (2007) J Electrochem Soc 154: A910–A916
27. ChiuHuang CK, Huang HYS (2013) J Electrochem Soc 160: A2184–A2188
28. ChiuHuang CK, Zhou C, Huang HYS (2014) J Nanotechnol Eng Med 5:021002
29. Wang D, Wu X, Wang Z, Chen L (2005) J Power Sources 140:125–128
30. Goodenough JB, Kim Y (2010) Chem Mater 22:587–603
31. Mukhopadhyay A, Sheldon BW (2014) Prog Mater Sci 63:58–116
32. Malave V, Berger JR, Zhu H, Kee RJ (2014) Electrochim Acta 130: 707–717
33. Zhu M, Park J, Sastry AM (2012) J Electrochem Soc 159:A492–A498
34. Zhao Z, Pharr M, Vlassak JJ, Suo Z (2010) J Appl Phys 108: 073517
35. Zhang X, Sastry AM, Shyy W (2008) J Electrochem Soc 155: A542–A552
36. Bower AF, Guduru PR (2012) Modell Simul Mater Sci Eng 20: 045004
37. Huang HYS, Wang YX (2012) J Electrochem Soc 159:A815–A821
38. Stamps MA, Eischen JW, Huang HYS (2015) J Eng Mech: under review
39. Lim C, Yan B, Yin L, Zhu L (2012) Electrochim Acta 75:279–287
40. Woodford WH, Carter WC, Chiang YM (2012) Energy Environ Sci 5:8014–8024

41. Woodford WH, Chiang YM, Carter WC (2010) J Electrochem Soc 157:A1052–A1059
42. Bohn E, Eckl T, Kamlah M, Mcmeeking R (2013) J Electrochem Soc 160:A1638–A1652
43. Nagpure SC, Downing RG, Bhushan B, Babu SS, Cao L (2011) Electrochim Acta 56:4735–4743
44. Monastyrskii MI (1999) Riemann, topology, and physics. Birkhäuser, Boston
45. Howell D (2006) Annual progress report—Energy Storage Research and Development, Washington D.C.
46. Morgan D, Ven AVD, Ceder G (2004) Electrochem Solid-State Lett 7:A30–A32
47. Farkhondeh M, Delacourt C (2012) J Electrochem Soc 159:A177–A192
48. Deshpande R, Qi Y, Cheng YT (2010) J Electrochem Soc 157: A967–A971
49. Maxisch T, Ceder G (2006) APS Phys Rev B: Condens Matter Mater Phys 73:174112
50. Brunetti G, Robert D, Guillemaud PB, Rouviere JL, Rauch EF, Martin JF, Colin JF, Bertin F, Cayron C (2011) ACS Chem Mater 23:4515–4524
51. Toonder JMJD, Dommelen JAWV, Baaijens FPT (1999) Modell Simul Mater Sci Eng 7:909–928
52. Daniel IM, Ishai O (2006) Engineering mechanics of composite materials. Oxford University Press, United Kingdom
53. Gabrisch H, Wilcox J, Doeff MM (2008) Electrochem Solid-State Lett 11:A25–A29
54. Park J, Lu W, Sastry AM (2011) J Electrochem Soc 158:A201–A206
55. Dathar GKP, Sheppard D, Stevenson KJ, Henkelman G (2011) ACS Chem Mater 23:4032–4037